2018

Defrost Cycle Optimization for Fan-Supplied Tube-Fin Evaporators Subjected to Frosting Conditions

Diogo Lôndero da Silva
Federal University of Santa Catarina, diogo.londero@ufsc.br

Christian Hermes
POLO Labs, Federal University of Santa Catarina, Brazil, hermes@polo.ufsc.br

Defrost Cycle Optimization for Fan-Supplied Tube-Fin Evaporators Subjected to Frosting Conditions

Diogo L. Da SILVA [1,*], Christian J. L. HERMES [2]

[1] Laboratory of Vehicular Refrigeration, Department of Mobility Engineering, Federal University of Santa Catarina, 89219-600, Joinville, SC, Brazil.

[2] POLO Research Laboratories, Department of Mechanical Engineering, Federal University of Santa Catarina 88040-900, Florianópolis, SC, Brazil.

[*]Corresponding author: diogo.londero@ufsc.br

ABSTRACT

Frost accretion on a tube-fin evaporator surface raises its thermal and hydraulic resistances, which in turn deteriorates the cooling capacity of the refrigeration system. For this reason, periodic defrost operations are required to recover the initial performance of the system. Most defrost techniques rely on supplying heat to the frost layer. Due to technological and thermodynamic limitations, only part of the heat supply is effectively used to melt the frost built-up on the evaporator, while the rest increases the refrigerator thermal load. Therefore, the amount of heat dissipated, the duration of a defrost operation, and the time between two consecutives defrost operations must be considered for properly designing the defrost system. The present paper assesses, by means of a simulation model that considers the airflow reduction with frost accretion, the effects of evaporator operating and geometric conditions, and defrost cycle parameters on the time-averaged cooling capacity. The results pointed out the existence of an optimum time for the defrost operation, indicating that short intervals between two defrost operations increase the thermal load by frequent heat supply, whilst long intervals promote severe capacity depletion by frost clogging.

1. INTRODUCTION

Most refrigeration systems operating under frosting conditions are equipped with fan-supplied tube-fin evaporators, where a frost layer, comprised of ice crystals and moist air, increases both the thermal and the hydraulic resistances of the coil. Such a double penalty reduces the cooling capacity of the refrigeration system, resulting in larger compressor runtime to accomplish the desired cooling demand. To retrieve the original (frost free) cooling capacity, periodic defrost operations are carried out by distinct strategies, such as hot-gas cycle, electric heating, continuous fan operation, low-frequency oscillation and ultrasonic vibration, among others (Welling *et al.* 2008; Amer and Wang, 2017). Hot-gas cycles and electric heating – commonly used in light commercial refrigeration and heat pumps – rely on supplying heat to melt the frost layer. Nonetheless, only a small part of the heat dissipated is effectively delivered to the frost layer, while a significant amount increases the refrigerator thermal load. Thus, parameters such as the amount of heat dissipated, the duration of a defrost operation, and the time between two consecutives defrost operations must be accounted for the design of the defrost system.

The open literature is abundant in studies that consider the role of defrosting on the performance of refrigeration systems. Sanders (1974) investigated, in his pioneering work, the influence of the evaporator defrost on the cooling capacity and the energy consumption. He observed that there is an optimum time between two consecutives defrost operations that reduces the energy consumption. A decade later, Zakrzewski (1984) analyzed, by means of a simplified defrost model, the effect of the frost layer on the depletion of the effective cooling capacity – defined as the difference between the energy removed by the evaporator during the compressor runtime, and the energy dissipated by the defrost system that is not effectively used for melting the ice. Machielsen and Kerschbaumer (1989) revisited Zakrzewski's formulation, proposing two dimensionless parameters related to the effective cooling capacity during a complete cycle of operation, and the average energy required to carry out the defrost process –

which allowed the determination of the optimum operating time for defrost. Radcenco *et al.* (1995) put forward a thermodynamic model to account for the effects of evaporator frosting and defrosting on the performance of a refrigerator, observing an optimum runtime that minimizes the inverse of the system COP. Some recent studies have also put their focuses on the defrost process. For instance, Zhu *et al*. (2015) investigated the operation of heat pumps and developed a defrost map from experimental results aiming at the time for defrosting as a function of the operating conditions, such as the air temperature and the relative humidity. Steiner and Rieberer (2015) numerically investigated the effect of the defrost operation in heat pump systems designed for electric vehicles, reporting that the temperature difference between the air and the refrigerant streams affects the ideal time for defrosting, and so the maximum system COP.

Other strategies to mitigate the negative effects of evaporator frosting have also been investigated. Song *et al.* (2016) carried out an experimental investigation on heat pump systems showing that a more uniform frost mass distribution decreases the time required for defrosting the coil, and so the required energy to melt the ice. They proposed a criterion based on the so-called frosting evenness value, a parameter that evaluates the frost mass distribution on the coil surface. Wang *et al.* (2017) compared the defrost performances of superhydrophobic, hydrophilic and bare finned-tube heat exchangers. Experiments were carried out to evaluate the defrost time, energy consumption, and retained water mass. The results showed that the superhydrophobic surface not only reduced the energy requirements for defrosting by 50%, but also the water retention after defrosting. Li *et al.* (2017) developed a numerical procedure to evaluate the accumulated frost mass, defrost heating and air flow distributions. The mathematical model was used to optimize the geometry of the air duct and baffle locations to match the frost mass and the defrost heat distributions on the evaporator surface. The numerical results were validated with experimental data and an increase of almost 30% in the defrost efficiency was obtained.

As evidenced in the literature review, a robust evaporator design for frosting conditions must take into account both the geometric parameters (e.g., tubes and fins) and the operating conditions (e.g., air and evaporator temperatures, air humidity, and air flow), which affect the heat and mass transfer rates, and hence the frost formation process, which in turn is related to the operating time until the evaporator gets blocked. The objective of present work is to investigate the effects of the frost accumulation and the defrost cycle on fan-supplied tube-fin evaporators. For doing so, a simulation model developed by the authors (Da Silva *et al*., 2011b and 2017), that considers the airflow reduction was used together with an approach developed by Zakrzewski (1984) to investigate the effects of frost accretion and the design parameters that lead to the optimal defrost cycle for fan-supplied tube-fin evaporators.

2. FROST BUILD-UP MODEL

The evaporator frosting model considers each row of tubes as a control volume. Moreover, the following simplifications are used: (i) diffusion of moisture and heat in the frost layer are considered quasi-steady; (ii) the frost layer thickness is uniform over the control volume; (iii) the Chilton-Colburn analogy for heat and mass transfer is applicable; and (iv) the thermophysical properties of air were considered uniform at each control surface (Da Silva *et al*., 2011b). Performing energy and mass balances on and within the frost surface, the following equation can be derived for calculating the frost surface temperature, T_s:

$$T_s = T_w + \frac{\left(\dot{Q}_{sen} + \dot{Q}_{lat}\right)}{A_s}\frac{x_f}{k_f} - \frac{\rho_a \omega_{sat,w} i_{sv}}{k_f}\frac{D\varepsilon}{\tau}\left[\frac{\omega_{sat,s}}{\omega_{sat,w}} - 1\right] \tag{1}$$

where A_s is the total heat transfer surface, x_f and k_f are the thickness and the thermal conductivity of the frost layer, respectively, i_{sv} is the latent heat of sublimation of ice, D is the diffusivity of water vapor in air, and ε and τ are the frost porosity and tortuosity, respectively. The frost accretion rate, the sensible and latent heat transfer rates, and the air side pressure drop are calculated, respectively, from the following equations (Da Silva *et al*., 2011b):

$$\dot{m}_f = \rho_a \dot{V}\left(\omega_{sat,s} - \omega_i\right)\left[1 - exp\left(-\frac{\eta_s A_s h_o}{\rho_a c_{p,a} \dot{V}\left(Le\,\tau/\varepsilon\right)^{2/3}}\right)\right] \tag{2}$$

$$\dot{Q}_{sen} = \rho_a \dot{V} c_{p,a} (T_s - T_i) \left[1 - exp\left(- \frac{\eta_s A_s h_o}{\rho_a c_{p,a} \dot{V}} \right) \right] \tag{3}$$

$$\dot{Q}_{lat} = \dot{m}_f i_{sv} \tag{4}$$

$$\Delta p = 2 C_f \rho_a \frac{L}{D_h} \left(\frac{\dot{V}}{A_{min}} \right)^2 \tag{5}$$

where the correlations proposed by Wang *et al*. (2000) for the heat exchangers characteristics were used to evaluate the convective heat transfer coefficient h_o, and the friction factor C_f. To simulate the performance of an axial fan typical of light commercial refrigeration systems, the airflow rate was calculated as a function of the evaporator air pressure drop (Da Silva *et al*. 2011a) previously obtained from Eq. (5). Such an approach relies on an iterative procedure, which varies the air flow rates accordingly (Da Silva *et al*. 2011b).

Moreover, the mass conservation principle was used to calculate the growth rate of the frost layer as follows:

$$\frac{dx_f}{dt} + \frac{x_f}{\rho_f} \frac{d\rho_f}{dt} = \frac{\dot{m}_f}{\rho_f A_s} \tag{6}$$

which requires an empirical correlation of the frost density, written as a function of the surface temperature and the air stream dewpoint, as follows:

$$\rho_f = \alpha exp(\beta T_s + \lambda T_{dew}) \tag{7}$$

where the coefficients are α = 494 kg m^{-3}, β = 0.11°C^{-1}, and λ = -0.06°C^{-1} (Da Silva *et al*., 2011b). Deriving equation (7) and substituting into equation (1) yields:

$$\frac{d\rho_f}{dt} = \frac{d\rho_f}{dT_s} \frac{dT_s}{dx_f} \frac{dx_f}{dt} \cong \beta \rho_f \left(\frac{\dot{Q}_{sen} + \dot{Q}_{lat}}{A_s k_f} \right) \frac{dx_f}{dt} \tag{8}$$

Now substituting equation (8) into equation (6), the following expression for the frost thickness can be obtained:

$$x_f(t + \Delta t) = x_f(t) + \int_t^{t+\Delta t} \frac{\dot{m}_f}{\rho_f A_s + \beta (x_f \rho_f / k_f)(\dot{Q}_{sen} + \dot{m}_f i_{sv})} dt \tag{9}$$

The evaporator frosting model was validated with experimental results, when it was observed that all numerical predictions fell within the experimental uncertainty bounds (Da Silva *et al*. 2011b).

3. DEFROST MODEL

The defrost model depends on the total mass of frost accumulated on the evaporator surface, calculated as follows:

$$M = \int_{t_{on}}^{t_{on}+t_{off}} \dot{m}_f dt \tag{10}$$

where t_{on} is refrigerator runtime and t_{off} is the defrost time, when the refrigeration system is switched off. The defrost efficiency is defined as the ratio between the exact energy amount needed to melt the ice, and the total energy

dissipated by the defrost system. Recognizing that the latent parcel is much larger than the sensible one, and that the defrost power $\dot{W}_d$ is constant over time, the defrost efficiency can be calculated from:

$$\eta_d = \frac{Mi_{sl}}{\dot{W}_d t_{off}} \tag{11}$$

It is important to highlight that part of the energy supplied by the heaters is not used to melt the ice, being dissipated in the refrigerator in the form of thermal load, $E_l = Mi_{sl}(1/\eta_d - 1)$. An empirical correlation based on experimental data of Mohs and Kulacki (2015) was used to calculate the defrost efficiency. The correlation is a function of the frost mass-to-surface area ratio, $m'' = M/A_s$, as originally proposed by Zakrzewski (1984):

$$\eta_d = m''(c_0 + c_1 m'') \tag{12}$$

where c_o = 1.285 [m^2 kg^{-1}] and c_1 = -0.5 [m^4 kg^{-2}]. Figure 1 compares equation (12) with the experimental data of Mohs and Kulacki (2015), where one can observe a fitting coefficient R^2~0.9 with most errors within the ±10% bounds.

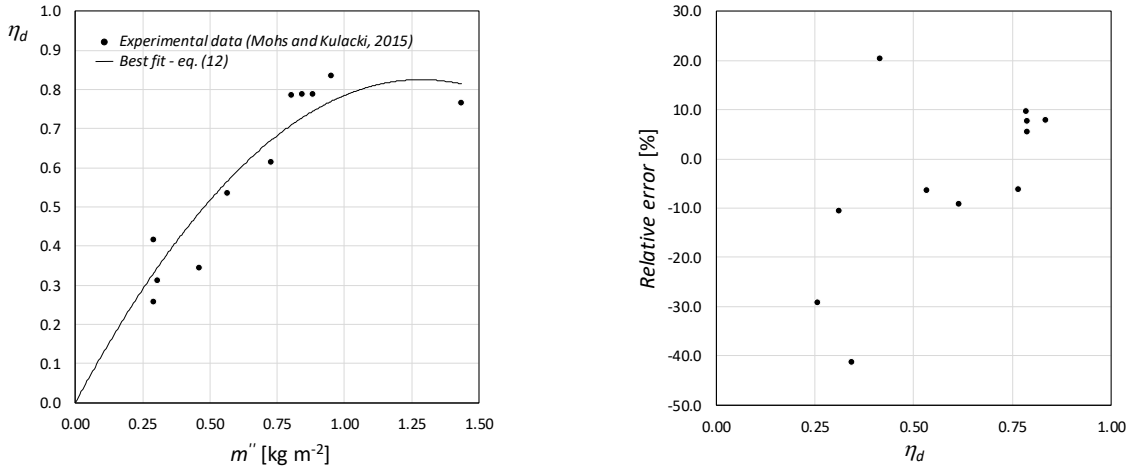

(a) (b)

Figure 1: Best fitting of defrost efficiency data of Mohs and Kulacki (2015)

The dataset of Mohs and Kulacki (2015) have 12 data points spanning coil surface temperatures from -20.2 to -9.6ºC, and air temperatures from -8.6 to 0.0ºC. The correlation is valid for frost mass-to-surface area ranging from 0.25 to 1.5, which covers the ones observed in the experimental study reported by Da Silva *et al*. (2011a). Equation (12) has a maximum defrost efficiency (≈83%) for $m'' \approx 1.25$ kg m^{-2}, a higher figure than the ones observed in the present study ($\lesssim 0.5$ kg m^{-2}).

The efficiency of the defrost cycle is defined as the ratio of the effective refrigerating capacity – the difference between the energy removed by the evaporator during the on cycle (t_{on}) and the energy dissipated by the defrost system during the off cycle (t_{off}) divided by the total time of the cycle – and the instantaneous cooling capacity of the clean (frost free) evaporator ($x_f \to 0$):

$$\eta_Q = \frac{\frac{1}{t_{on}+t_{off}} \int_{t_{on}}^{t_{on}+t_{off}} \left[\dot{Q}_{sen} + \dot{m}_f i_{sv} - \dot{m}_f i_{sl}\left(1/\eta_d - 1\right)\right] dt}{\lim_{x_f \to 0}\left(\dot{Q}_{sen} + \dot{Q}_{lat}\right)} \tag{13}$$

Equation (13) shows that the efficiency of the defrost cycle is related to the frost formation and defrost times, the frost accumulation rate, and the heat transfer rates in the evaporator.

4. RESULTS

A schematic representation of a typical tube-fin evaporator for light-commercial refrigeration applications is shown in Fig. 2. The numerical experimentation, including a sensitivity analysis, was performed using different values for the key input parameters of the model, as depicted in Table 1. The geometries G1 and G2 represent two evaporators with length, height and depth equivalent to 320 mm, 152 mm and 45 mm, respectively. The difference lies in the number of fins, 127 for the evaporator G1 and 168 for G2, which represents a surface area increase of 30% with respect to G1.

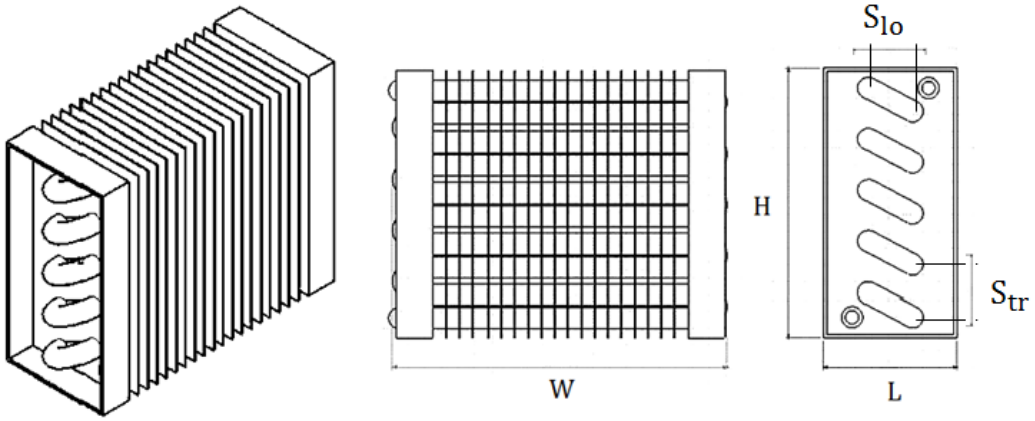

Figure 2: Schematic representation of the evaporator geometry with W=320 mm, H=152 mm, L=45 mm, N_{fin}=127 (G1) 168 (G2)

Table 1: Summary of geometries and operating conditions used in the numerical simulations

Case	Geometry	T_w [ºC]	T_a [ºC]	ϕ [%]	$\dot{W}_d''$ [W m^{-2}]
1	G1	-10.0	2.5	74	200
2	G1	-10.0	2.5	74	400
3	G1	-8.0	2.5	74	200
4	G1	-10.0	2.5	90	200
5	G2	-10.0	2.5	74	200
6	G2	-10.0	2.5	74	400
7	G2	-8.0	2.5	74	200
8	G2	-10.0	2.5	90	200

Figure 3.a shows the cooling capacity depletion over time, which is due to the combined effect of the air flow rate reduction and the increase in the thermal resistance associated with the frost layer. One can observe a steep decrease in the cooling capacity after 60 minutes, which is related to the stall region of the axial fan (Da Silva *et al.*, 2011b). Figure 3.b, on the other hand, shows the time required to perform the defrost process as a function of the cumulative system runtime. As predicted by equation (11), the defrost time increases with the amount of frost accumulated in the evaporator although presenting a small curvature due to the nonlinear behavior of the defrost efficiency, described by equation (12).

Figure 4 shows the defrost cycle efficiency, calculated from equation (13), as a function of runtime for the different cases of Table 1. In all cases there is an optimal time to start the defrost operation. For example, for case 1, one can observe that the optimal time to defrost occurs at 86 minutes, when the efficiency corresponds to 67%. Table 2 shows the optimal times for starting the defrost operation and the associated efficiency for all cases in Table 1.

The comparisons between cases 1 & 2 and 5 & 6 in Fig. 4 show that an increase in the defrost power reduces the defrost time, which in turn increases the defrost cycle efficiency, as can be verified in equation (13). This result is one of the reasons why refrigerators manufactures use relatively high power defrost heaters. Moreover, through the analysis of cases 1 & 3 and 5 & 7, one verifies that a higher evaporator temperature causes a significant increase in

the optimum time to start the defrost operation, thus increasing the defrost cycle efficiency. This behavior can be explained by the lower mass transfer rate (eqs. 2 and 4) and the higher frost density (eq. 7) observed for higher coil temperatures. To evaluate the effect of the psychrometric conditions at the evaporator inlet, different values of relative humidity were evaluated, as observed in cases 1 & 4 and 5 & 8 of Table 1. The comparison between these results shows that the increase of the relative humidity causes the reduction of the defrost cycle efficiency, which is mainly due to the increase of the mass transfer rate (eqs. 2 and 4) and the lower frost density (eq. 7).

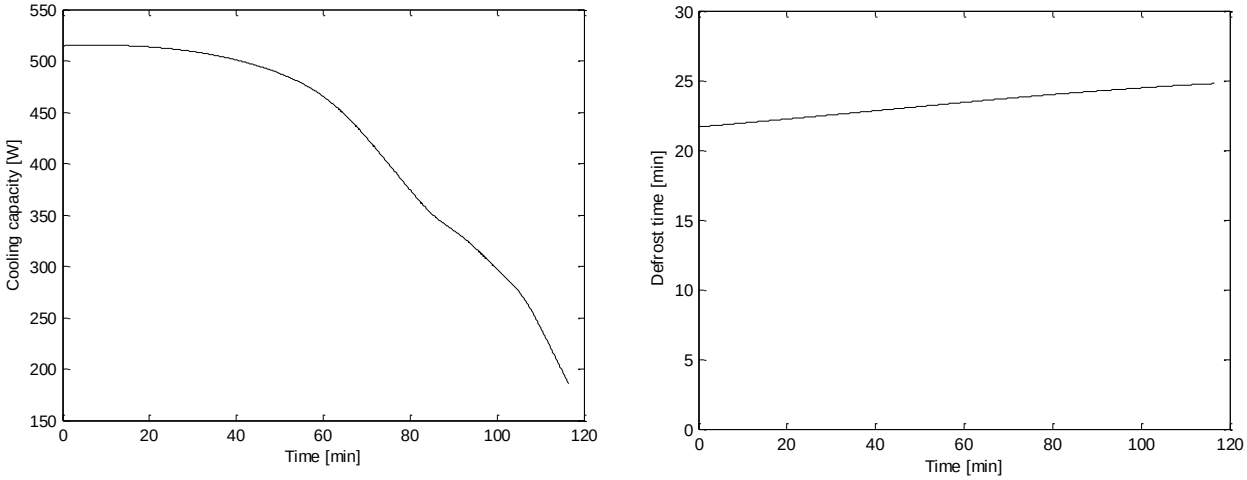

(a) (b)

Figure 3: Time evolution of (a) frost mass and (b) air flow rate - case 1

The combination of Figure 4 and Table 2 allow one to evaluate the effect of the geometry on the defrost cycle efficiency, and the optimal time to start the defrost operation. For example, the comparison of case 1 with case 5 shows that the change of the geometry from G1 to G2 causes a reduction in the optimal time to start defrosting from 86 to 69 minutes, while the maximum defrost cycle efficiency is reduced from 67% to 58%. Similar conclusions are obtained for other cases of Table 1, indicating that the increase in the fin density not only causes the reduction in the defrost cycle efficiency but also in the optimal time to start the defrost operation.

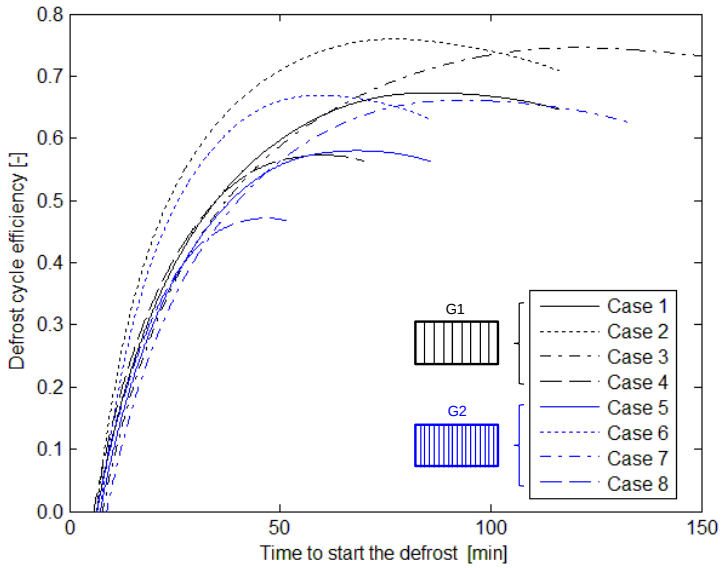

Figure 4: Comparison between the efficiency of the defrost cycle for the cases of Table 1

The evaporator geometry was additionally evaluated by comparing the evaporator G1 with a third one (G3) having the same fin spacing but a larger length (420 mm), which increases the surface area. In this analysis, 200 Wm^{-2} of defrost power was employed, while the temperature and relative humidity of the air at the evaporators inlet were maintained at 4°C and 85%, respectively. The operating temperatures of the evaporators G1 and G3 were selected as -10.0°C and -8.7°C, respectively, to maintain the same initial (frost free) cooling capacity.

Table 2: Comparison between optimum times to defrost and defrost cycle efficiencies

Case	Optimum time [min]	Defrost cycle efficiency [-]
1	86	0.67
2	78	0.76
3	121	0.74
4	60	0.57
5	69	0.58
6	60	0.67
7	92	0.66
8	47	0.47

Figure 5.a compares the accumulated frost mass for two different coil geometries as a function of time. The reduction in the frost accumulation rate observed for G1 is due to the reduction of the air flow because of the obstruction imposed by the frost build-up. The simulation of evaporator G1 finishes after 65 minutes, when the airflow reaches its minimum value (30 m^3h^{-1}). Since evaporator G3 has a larger surface area, it is capable of accumulating larger amounts of frost before the airflow reaches the minimum allowable figure. Although both geometries have the same initial cooling capacity, evaporator G3 is more robust under frosting conditions, as depicted in Fig. 5.b. For instance, after 30 minutes, when the two evaporators contain approximately 130 grams of frost, it is found that the cooling capacities of the evaporators G1 and G3 are equivalent to 582 W and 630 W, respectively. So, while the cooling capacity of evaporator G1 diminished by 8%, evaporator G3 experienced no performance depletion.

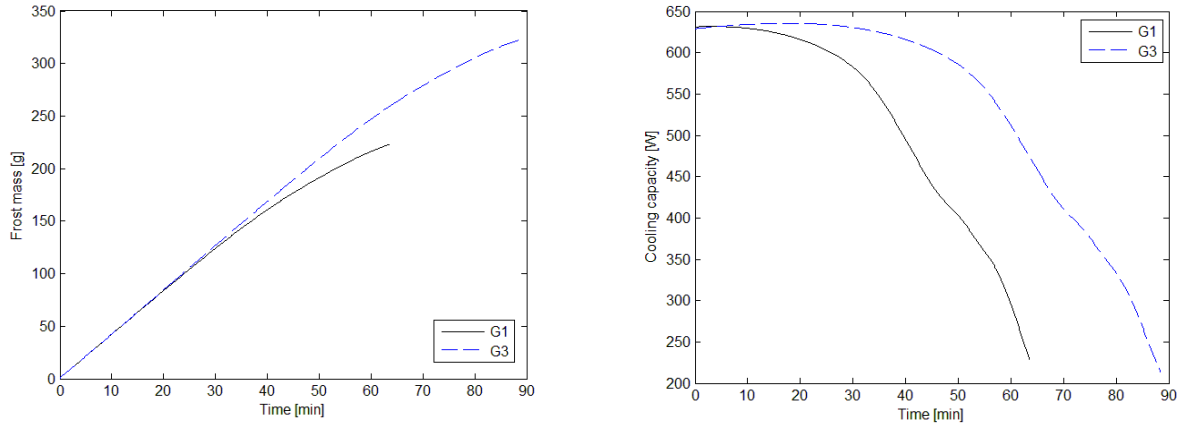

(a) (b)

Figure 5: Comparison between G1 and G3 geometries for (a) accumulated frost mass and (b) cooling capacity

Figure 6.a compares the capacity ratios of evaporators G1 and G3, defined here as the ratio between the instantaneous and the initial (frost free) cooling capacities. It is possible to verify a rapid degradation of the capacity ratio of evaporator G1 due to the fast obstruction by the frost layer. It should be noted that, in addition to having a smaller surface area to accommodate the frost layer, evaporator G1 also operates at a lower temperature, which reduces the frost density as predicted by equation (7). During the initial stages of the simulations, it is also observed that the capacity ratios of the evaporators are greater than 1, which are due to the increase in the evaporator *UA*, which can be explained by the increase of the surface area by frost deposition and the raise of the air velocity related to the reduction of the free flow area, thus increasing the heat transfer coefficient.

When the evaporator operates continuously for a certain period of time, it is necessary to carry out a defrost operation to retrieve the initial cooling capacity. The effect of the defrost time on defrost cycle efficiency is depicted in Figure 6.b. Again, the presence of an optimum is observed for both geometries. An analysis of the curves points out that the replacement of G1 by G3 raises the maximum defrost cycle efficiency from 55% to 64%. In addition, there is an increase in the optimum time for starting the defrost process for evaporator G3 in comparison with G1, which results in a reduction in the number of defrost operations.

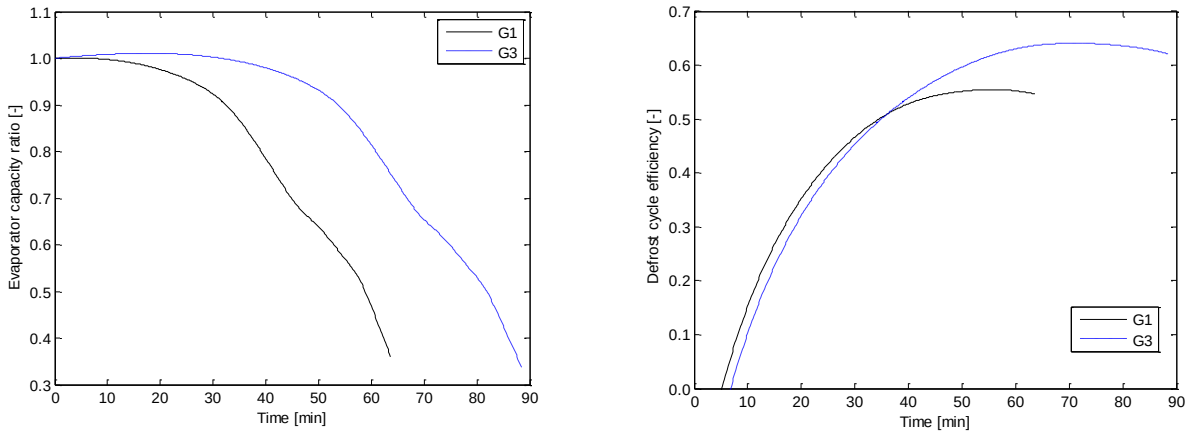

(a) (b)

Figure 6: Comparison between G1 and G3 geometries for (a) evaporator capacity ratio and (b) defrost cycle efficiency (eq. 13)

5. CONCLUSIONS

Simulations were performed considering different geometries and operating conditions for fan-supplied tube-fin evaporator running under frosting conditions. The results pointed out the existence of an optimum time for the defrost operation in which the maximum defrost cycle efficiency is obtained. It was observed that an increase in the defrost power and a reduction of the frost formation rate increase the defrost cycle efficiency. Furthermore, the performances of two evaporators with different geometries, but with the same initial (frost free) cooling capacity, were compared using different evaporating temperatures. This analysis evidenced the effect of the key geometric parameters on the efficiency of the defrost cycle and showed their influences on the number of defrost operations. Finally, this study highlights the need for a first-principles model for the defrost efficiency that accounts for the physical principles related to sublimation and melting of the frost layer, instead of the empirical regression used in the simulations.

NOMENCLATURE

Roman

A_s	surface area (m^2)
C_f	Fanning friction factor (-)
c_p	specific heat of moist air (J kg^{-1} K^{-1})
D	water vapor diffusivity on air (m^2 s^{-1})
E_t	total defrost energy (J)
E_l	energy losses (J)
E_d	effective defrost energy (J)
h_m	mass transfer coefficient (kg m^{-2} s^{-1})
h_o	heat transfer coefficient (W m^{-2} K^{-1})
i_{sl}	latent heat of solidification (J kg^{-1})
i_{sv}	latent heat of sublimation (J kg^{-1})
k	thermal conductivity (W m^{-1} K^{-1})
M	frost mass (kg)
$\dot{m}$	mass flow rate (kg s^{-1})
m''	frost mass to surface area ratio (kg m^{-2})
p	pressure (Pa)
$\dot{Q}$	heat flux rate (W m^{-2})
T	temperature (K)
t	time (s)
V	volumetric flow rate (m s^{-3})
$\dot{W}$	power (W)
x_f	frost thickness (m)

Greek

ε	porosity (-)
η	efficiency (-)
ϕ	relative humidity (-)
ρ	density [kg m^{-3}]
τ	tortuosity [-]
ω	humidity ratio (kg$_v$ kg$_a^{-1}$)

Subscripts

a	air
cv	control volume
d	defrost
dew	dew-point
f	frost
i	inlet
lat	latent
min	minimum
o	outlet
off	switched off
on	switched on
s	surface
sat	saturation
sen	sensible
v	vapor
w	wall

REFERENCES

Amer M, Wang CC, Review of defrosting methods, *Renewable and Sustainable Energy Reviews*, 73 (2017) 53–74.

Da Silva DL, Hermes CJL, Melo C, Effect of frost morphology on the thermal-hydraulic performance of fan-supplied tube-fin evaporators, *Applied Thermal Engineering*, 111 (2017) 1060-1068.

Da Silva DL, Hermes CJL, Melo C, Experimental study of frost accumulation on fan-supplied tube-fin evaporators, *Applied Thermal Engineering*, 31 (2011a) 1013-1020.

Da Silva DL, Hermes CJL, Melo C, First-principles simulation of frost accumulation on fan-supplied tube-fin evaporators, *Applied Thermal Engineering*, 31 (2011b) 2616-2621.

Hermes CJL, An analytical solution to the problem of frost growth and densification on flat surfaces, *International Journal of Heat and Mass Transfer*, 55 (2012) 7346-7351.

Hermes CJL, Piucco RO, Barbosa JR, Melo C, A study of frost growth and densification on flat surfaces, *Experimental Thermal and Fluid Science*, 33(2) (2009) 371-379.

Li Z, Zhao D, Ding G, Ren T, Miao S, Han X, Noda T, Improving defrost performance by controlling frost distribution to match defrost heat distribution in frost-free household refrigerators, *International Journal of Refrigeration*, 77 (2017) 136-148.

Machielsen CHM, Kerschbaumer HG, Influence of frost formation and defrost on the performance of air coolers: standards and dimensionless coefficients for the system designer, *International Journal of Refrigeration*, 12 (1989) 283-290.

Mohs WF, Kulacki FA, *Heat and Mass Transfer in the Melting of Frost*, Springer, 97p, 2015.

Radcenco V, Bejan A, Vargas JVC, Lim JS., Two design aspects of defrost refrigerators, *International Journal of Refrigeration*, 18 (1995) 76-86.

Sanders CT, Frost Formation: *The influence of frost formation and defrost on the performance of air coolers*, PhD Thesis, Delft University of Technology, 1974.

Song M, Mao N, Deng S, Xia Y, Chen Y, An experimental study on defrost performance for an air source heat pump unit at different frosting evenness values with melted frost local drainage, *Applied Thermal Engineering*, 99 (2016) 730–740.

Steiner A, Rieberer R, Simulation based identification of the ideal defrost start time for a heat pump system for electric vehicles, *International Journal of Refrigeration*, 57 (2015) 87-93.

Wang CC, Chi KY, Chang CJ, Heat transfer and friction characteristics of plain fin-and-tube exchangers, Part II: Correlation, *International Journal of Heat and Mass Transfer*, 43 (2000) 2693-2700.

Wang F, Liang C, Zhang Y, Zhang X, Defrost performance of superhydrophobic fin-tube heat exchanger, *Applied Thermal Engineering*, 113 (2017) 229–237.

Wellig B, Imholz M, Albert M, Hilfiker K, Defrosting the fin tube evaporators of air/water heat pumps using ambient air, *9th International IEA Heat Pump Conference*, 20 – 22 May 2008, Zürich, Switzerland.

Zakrzewski B, Optimal defrost cycle for the air cooler, *International Journal of Refrigeration*, 7 (1984) 41-45.

Zhu JH, Sun YY, Wang W, Deng SM, Ge YJ, Li LT, Developing a new frosting map to guide defrost control for air source heat pump units, *Applied Thermal Engineering*, 90 (2015) 782-791.

ACKNOWLEDGEMENTS

This study was carried out under the auspices of the Brazilian Government funding agencies CAPES and CNPq.